Energy & Environmental Science

ROYAL SOCIETY OF CHEMISTRY

PAPER

View Article Online
View Journal | View Issue

Cite this: *Energy Environ. Sci.*, 2025, **18**, 7928

Balancing solvation: stabilizing lithium metal batteries *via* optimized cosolvents for ionic-liquid electrolytes†

Xinlin Li,[a] Xianyang Wu,[a] Seoung-Bum Son,[a] Jorge Seminario, *[bde] Perla Balbuena, *[bef] Anderson Arboleda,[b] Jiyu Cai, [a] Matthew Li,[a] Ziyuan Lyu,[gh] Dominic Bresser, [gh] Rachid Amine,[c] Chi-Cheung Su *[a] and Khalil Amine *[a]

In this study, we examined three cosolvents with distinct solvation capabilities for ionic-liquid electrolytes based on 1-methyl-1-propyl pyrrolidinium bis(fluorosulfonyl)imide (**Py13FSI**). We demonstrate that 1,1,1-trifluoro-2-(2-(2-(2,2,2-trifluoroethoxy)ethoxy)ethoxy)ethane (**FDG**) notably enhances the cycle life of **Py13FSI**-based electrolytes, outperforming 1,1,2,2-tetrafluoroethyl 2,2,3,3-tetrafluoropropylether (**TTE**) and diglyme (**DG**). Electrochemical and surface analyses showed that this improvement could be attributed to the formation of a favorable cathode interphase, promoting efficient Li^+ transport with reduced overpotential. Spectroscopic techniques (FTIR, Raman, and NMR spectroscopy) and molecular dynamics simulations revealed that cosolvents with varying solvation abilities can influence the solvation structures in **Py13FSI**-based electrolytes. The mild solvating strength and lithium stability of **FDG** are key contributors to its effectiveness. Conversely, **DG**, a strong solvating solvent, destabilized the **Py13FSI**-**DG** electrolyte at the lithium metal anode, while **TTE**, a non-solvating solvent, failed to enhance lithium transport or form a stable cathode interphase. Our findings highlight that balanced solvation exerted by the cosolvents is critical for forming a stable electrolyte–cathode interface, potentially through FSI decomposition. This study offers valuable insights into the development of durable ionic-liquid electrolytes, emphasizing the importance of selecting cosolvents with optimal solvation properties.

Received 17th March 2025,
Accepted 17th June 2025

DOI: 10.1039/d5ee01515d

rsc.li/ees

Broader context

Ionic liquid-based electrolytes, particularly those containing **Py13FSI**, have attracted attention for their potential to enhance the performance of lithium metal batteries (LMBs) due to their stability and non-flammability. However, a major challenge in advancing these electrolytes is achieving a stable and efficient electrolyte–cathode interface. This study highlights the role of co-solvents, specifically **FDG**, in optimizing the solvation environment to improve battery performance. By stabilizing the cathode interphase and promoting efficient Li^+ transport with reduced overpotential, **FDG** significantly extends the cycling life. Our findings emphasize the importance of balancing solvation properties when designing new electrolytes, as a medium-range solvation shell is crucial for forming a stable electrolyte–cathode interface. This work provides valuable insights into the design of future electrolytes by carefully selecting co-solvents that balance solvating capabilities, offering a pathway to developing more durable and high-performance electrolyte systems.

[a] *Chemical Sciences and Engineering Division, Argonne National Laboratory, 9700 S. Cass Avenue, Lemont, IL 60439, USA*
[b] *Department of Chemical Engineering, Texas A&M University, College Station, Texas, 77843, USA. E-mail: csu@anl.gov, seminario@tamu.edu, balbuena@tamu.edu, amine@anl.gov*
[c] *Materials Science Division, Argonne National Laboratory, 9700 S. Cass Avenue, Lemont, IL 60439, USA*
[d] *Department of Electrical and Computer Engineering, Texas A&M University, College Station, Texas, 77843, USA*
[e] *Department of Materials Science and Engineering, Texas A&M University, College Station, Texas, 77843, USA*
[f] *Department of Chemistry, Texas A&M University, College Station, Texas, 77843, USA*
[g] *Helmholtz Institute Ulm (HIU), Electrochemical Energy Storage, 89081 Ulm, Germany*
[h] *Karlsruhe Institute of Technology (KIT), 76021 Karlsruhe, Germany*

† Electronic supplementary information (ESI) available. See DOI: **https://doi.org/10.1039/d5ee01515d**

Introduction

Lithium metal batteries (LMBs) represent a promising frontier in the realm of energy-storage technologies owing to their exceptionally high theoretical capacity (3860 mAh g^{-1}) and very low redox potential (−3.04 V *vs.* SHE).[1,2] The synergistic utilization of a lithium-metal anode alongside a nickel-rich cathode material, such as $LiNi_{1-x-y}Mn_xCo_yO_2$ (NMC), stands out as one of the most promising combinations for attaining high-energy-density batteries.[3–5] However, the highly oxidative NMC and highly reductive lithium anode pose challenges to the robustness of electrolytes, which are vulnerable to parasitic degradations at electrolyte–electrode interfaces. The reversibility of lithium plating/stripping heavily relies on the electrochemical stability of passivation interphases formed on the cathode and anode during cycling.[6–10] Although excellent overall cell performance has been demonstrated, state-of-the-art organic electrolytes exhibit unsatisfactory coulombic efficiency, capacity retention, and safety concerns due to their low cathodic/anodic stability in LMBs and their high flammability.[11,12]

Extensive efforts have been devoted to developing promising electrolyte systems that can overcome the aforementioned issues in LMBs, such as highly concentrated[13–16] and localized-high-concentration electrolytes.[17–20] Among the large variety of potential solvents capable of solvating lithium ions, ionic liquids (**ILs**), a class of salts existing in the liquid state at ambient temperature with negligible vapor pressure, have emerged as a compelling alternative to conventional organic solvents because of their remarkable solvation capability for Li^+ (*i.e.* typically in the form of lithium bis(fluorosulfonyl)imide (LiFSI) or bis(trifluoromethylsulfonyl)imide (LiTFSI)s), electrochemical stability, and low flammability.[21–26] The broad electrochemical windows of various **ILs** suggest they could be promising solvents in electrochemical applications including lithium batteries.[27,28] Despite the high cycling stability of IL electrolytes in LMBs, as revealed by recent research, their overall cell performance is limited by their intrinsically high viscosity and sluggish Li^+ transport. Therefore, electrolyte engineering, typically through the incorporation of cosolvents that can modulate solvation structures and reduce overall viscosity, which could be beneficial for interfacial stability, is regarded as a highly promising and effective approach to enhance ionic conductivity and, ideally, cycling stability.[22,29–31]

Steric hindrance from the IL cation makes it less favorable to be included in the close solvation shell than the dissolved Li^+ with a smaller ionic radius.[32] The solvation sheath is therefore mainly comprised of Li^+ and FSI anions in pristine IL electrolytes.[33–35] Among the reported cosolvents, those with strong solvating capabilities, such as carbonates and ethers, usually intervene in Li ions' solvation with FSI anions, which is unfavorable for the formation of stable interphases in LMBs.[29,30] Non-solvating cosolvents, such as 1,1,2,2-tetrafluoroethyl 2,2,3,3-tetrafluoropropylether (**TTE**) and bis(2,2,2-trifluoroethyl) ether (**BTFE**), which are electrochemically stable in cellular environments, offer new possibilities to overcome the challenges of IL-based electrolytes. In particular, they can significantly reduce the total viscosity of the IL electrolyte without participating in a straightforward solvation of the lithium complexes.[22,29,30] However, the addition of non-solvating solvents may alter lithium's overall solvating ability and the dielectric constant of the electrolyte solvents, which could further affect lithium transport.[30,31] Thus, it is challenging to balance the cosolvents' solvation capabilities, oxidation/reduction stability, and physical properties, such as viscosity and ionic conductivity (especially lithium transport capability), in IL-based electrolytes to achieve optimal cell performance.

Herein, we developed an electrolyte system comprised of the IL 1-methyl-1-propyl pyrrolidinium bis(fluorosulfonyl)imide (**Py13FSI**), and the fluorinated diethylene glycol ether 1,1,1-trifluoro-2-(2-(2-(2,2,2-trifluoroethoxy)ethoxy)ethoxy)ethane (**FDG**) as the optimal solvating cosolvent, which demonstrated excellent capacity retention in Li||NMC811 ($LiNi_{0.8}Mn_{0.1}Co_{0.1}O_2$) cells. To the best of our knowledge, this is the first demonstration of incorporating a glycol ether-type cosolvent into an IL-based electrolyte in an LMB. Comparison among three distinct cosolvents, *i.e.*, diglyme (**DG**), **FDG**, and **TTE**, which have descending lithium-solvating capabilities, allowed distinguishing the unique electronic and solvation properties of **FDG** compared to the other cosolvents in order to obtain an enhanced capacity retention in LMBs. The results show that **FDG**, with its suitable lithium-solvating ability and appropriate electrochemical stability window, could serve as the optimal cosolvent for IL-based electrolytes. Li||NMC811 cells were fabricated using the **Py13FSI-FDG** electrolyte and displayed a significantly reduced overpotential for Li intercalation into the NMC cathode upon long-term cycling and enhanced capacity retention compared to the other formulations. These results strongly suggest that both the electrolyte–anode and electrolyte–cathode interphases were stabilized in the **Py13FSI-FDG** cell, as evidenced by the findings from electrochemical and surface analyses. Moreover, the beneficial effect of incorporating **FDG** into the electrolyte was also evident in the stabilization of the cathode–electrolyte interphase (CEI), achieved through the alteration of the solvation sheath, as indicated by the molecular dynamics (MD) simulation results.

Results and discussion

Study of the solvation structures enabled by the different cosolvents

The electrolytes were formulated by dissolving 1.4 m (molality, mol/kg) LiFSI in a liquid phase comprising **Py13FSI** and the desired cosolvents in a volumetric ratio of 4 : 1. Three cosolvents with distinct solvating capabilities, as reflected by their molecular electrostatic potential (**MEP**) (Fig. 1a) and oxidation/reduction potential (as indicated by their HOMO and LUMO energies, Fig. 1b), were utilized in this work. Viscosity measurements (Fig. S1 and S2, ESI†) were performed and manifested the reduction in viscosity upon the addition of cosolvents from 77 cP in the neat **Py13FSI** electrolyte to 45 and 54 cP at 20 °C in **Py13FSI** + **TTE** and **Py13FSI** + **FDG**, respectively. The solvation structures of the IL-based electrolytes were experimentally

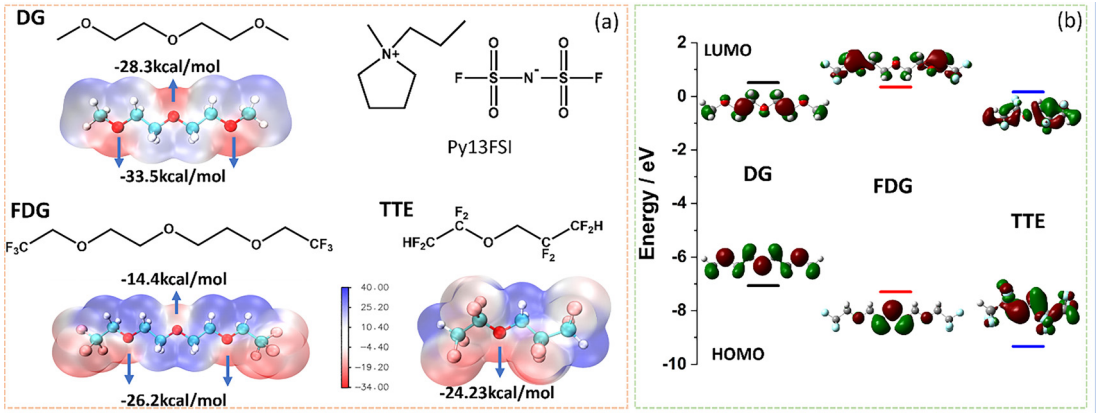

Fig. 1 (a) Structures of **Py13FSI** and cosolvents and the calculated molecular electrostatic potential (**MEP**) on isodensity surfaces of **DG**, **FDG**, and **TTE**, showing the negative (red) and positive (blue) regions; (b) calculated HOMO and LUMO energies and wavefunctions of the three cosolvents.

studied *via* Fourier transform infrared (FTIR) (Fig. 2a), Raman (Fig. 2b), and NMR (Fig. 2c) spectroscopies. The IR absorption in the 800–880 cm^{-1} range (this range was targeted due to the noninterference by cosolvents) highlighted the S–N–S asymmetric stretching from the FSI anion (Fig. 2a). Dissolving 1.4 m LiFSI in **Py13FSI** resulted in a peak shift from 825 to 834 cm^{-1}, underscoring the sulfonyl groups' coordination with the Li^+ ions (Fig. 2a and 2d). Compared with the absorption at 834 cm^{-1} in 1.4 m LiFSI **Py13FSI** + **TTE**, the addition of **TTE** and **FDG** did not cause a noticeable absorption shift. However, introducing **DG** led to an absorption shift closer to the **Py13FSI** absorption (without LiFSI) at 828.5 cm^{-1}, which suggested a strong solvation of Li^+ by **DG** (Fig. 2e), which then increases the portion of non-solvated FSI anions.

To further investigate the solvation capabilities of the different cosolvents, especially **FDG** and **TTE**, we conducted Raman spectroscopy focusing on the sulfonyl vibration (700–780 cm^{-1}) in the four electrolytes (Fig. 2b). There was a 17 cm^{-1} absorption shift from the IL (725 cm^{-1}) to the **Py13FSI** electrolyte with 1.4 m LiFSI (742 cm^{-1}) due to Li^+ coordination with

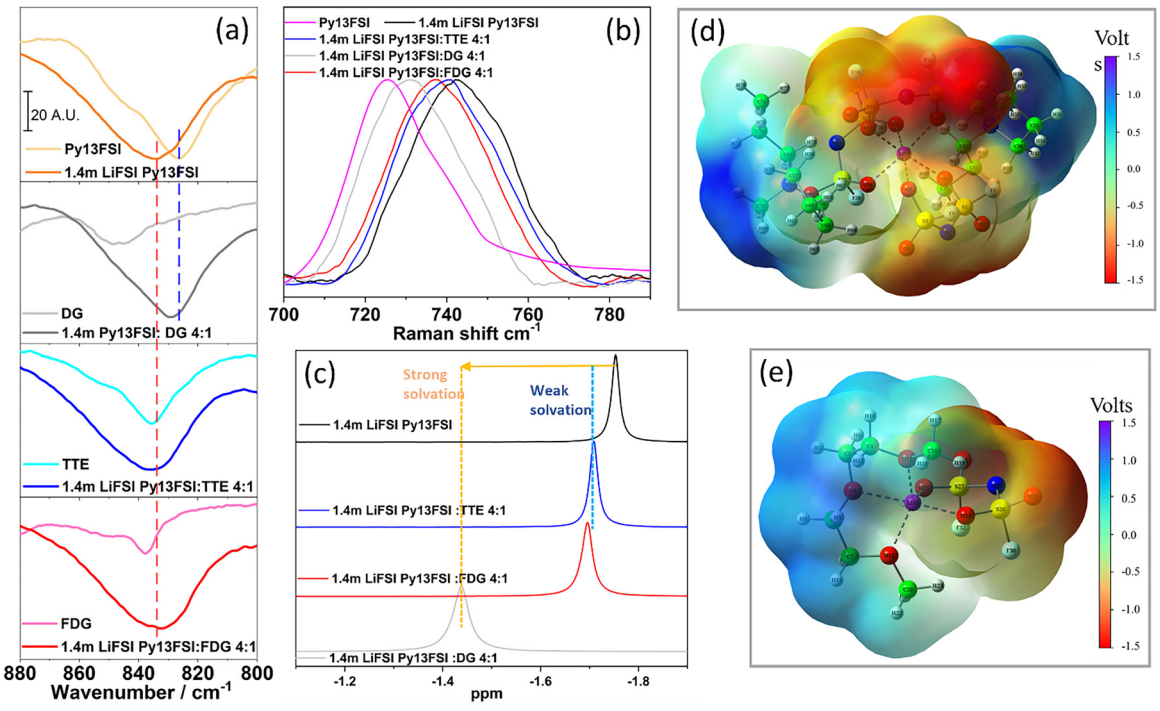

Fig. 2 (a) FTIR spectra for the four electrolytes in the wavenumber range showing S–N–S asymmetric stretching from the FSI anion. Absorption of cosolvents at the same range were plotted to show their noninterference of the S–N–S signal in the electrolyte. (b) ^7Li NMR spectra for the four electrolytes revealing the chemical environment of Li^+ in the solvation sheath. (c) Raman spectra for the four electrolytes through probing S–N–S asymmetric stretching from the FSI anion. *Ab initio*-Optimized structures of a cluster depicting (d) the coordination between **DG**/FSI^- and Li^+ and the corresponding **MEP** surface, and (e) the coordination between FSI^- and Li^+ and the corresponding **MEP**.

the FSI anion. Similar to the IR data, adding **DG** led to an absorption shift to lower wavenumbers, namely at about 730 cm^{-1} (*i.e.* closer to **Py13FSI** without lithium salt), indicating the strong solvation capability of **DG** (Fig. 2e), which reduced the coordination ratio between FSI and Li^+. In contrast, the minimal shift toward lower wavenumbers (737 and 740 cm^{-1}) relative to 1.4 m LiFSI **Py13FSI** at 740 cm^{-1} caused by **FDG** and **TTE** revealed their moderate solvation capabilities. The relatively smaller shift of **TTE** suggested its lower solvation power compared to **FDG**. Note that the non-solvating nature of **TTE** has been previously reported in localized-high-concentration electrolytes as a diluent.[3,20] To further verify the solvation capabilities of the cosolvents, we probed the chemical environment of Li^+ ions through ^7Li NMR spectroscopy. The coordination between **DG** and Li^+ significantly shifted the ^7Li signal toward the high field, as observed in Fig. 2c, whereas the use of low-solvating-power **TTE** and **FDG** as cosolvents, which exert weak interactions with Li^+, exhibited a lesser shift of the ^7Li signal. The lesser shift stemming from **FDG** than **TTE** also indicated **FDG**'s higher solvation power than **TTE**, which was in good agreement with the Raman data. The strong solvation exerted by **DG** would increase its population in the inner solvation sheath surrounding Li^+, and would bring significant **DG**-electrolyte features (*i.e.*, a poor cycling stability in LMBs) over the relatively stable cycling feature of the neat IL-based electrolyte.

To gain further insights into the solvation structures, classic molecular dynamic (MD) simulations were carried out to visualize the solvation structures of these IL-based electrolytes. The snapshots in Fig. 3a–c demonstrate that Li^+ closely interacted with FSI^- clouds in the solvation sheath, while positioning $Py13^+$ cations at the peripheral distance. The introduction of cosolvents (blue clouds) affected the solvation sheath to different extents due to their varied electronic and solvating properties. The radial distribution function (RDF, Fig. 3d) was assessed and revealed the distribution of several ion pairs between Li cations and FSI anions and oxygens from the cosolvents. The RDF of Li–O_{FSI} (Fig. S3, ESI†) showed a modest difference in the inner shell (2.0–2.4 Å) of all four electrolytes due to the relatively low concentration of LiFSI salt and the low volumetric percentage (20%) of the cosolvents. The saturation number of five in the 2–3 Å range observed in the cumulative number analysis (Fig. 3f) indicated a coordination number of five, mostly between Li^+ and FSI^-, in all the targeted electrolytes. From the cosolvent aspect; however, the RDFs of Li–O_{DG}, Li–O_{TTE}, and Li–O_{FDG} exhibited noticeable differences in the medial range of 3.0–6.0 Å. The two broad peaks centered at 3.5 and 5.3 Å in the Li–O_{DG} spectrum manifested that **DG** formed two shells outside the inner sheath constituted by Li^+ and FSI^- due to its strong solvation capability. In contrast, **FDG** and **TTE** exhibited weaker solvation powers, as indicated by their RDF peaks occurring at a farther distance of 5–6 Å. The *ab initio* calculation results in Fig. 3g and h depict the relative positions of the Li^+, FSI^-, and cosolvents (*i.e.*, Li^+ and the cosolvents did not show a direct coordination). The lower onset of the Li–O_{FDG} RDF peak than that of Li–O_{TTE} verified the weaker solvation power of **TTE**, which well agreed with the Raman and NMR results. The cumulative distribution of the cosolvents (Fig. 3e) further confirmed the order of solvation power as **DG** > **FDG** > **TTE** by the descending population from **DG**, **FDG**, to **TTE** in the radial range of 4–6 Å. Our solvation study along with electrochemical results provided evidence that the solvation differences across these four electrolytes had a significant influence on lithium plating/stripping and interphase formation, which will be covered in the sections below.

Facilitating lithium plating/stripping with the FDG cosolvent

Given the distinct solvation capabilities enabled by different cosolvents, our next goal was to evaluate the lithium plating/stripping efficiency in these IL-based electrolytes. We first monitored the time-lapsed voltage profiles in symmetric Li||Li cells when applying a current density of 1 mA cm^{-2}. It was evident that **Py13FSI** and **Py13FSI** + **DG** displayed significant polarization, whereas **TTE** and **FDG** could help stabilize Li cycling, as evidenced by the lower and more stable polarization observed (Fig. 4d). The efficiency of the Li plating/stripping process was also assessed through measuring the coulombic efficiency (CE) of Li||Cu cells (Fig. 4a–c). The Li||Cu cells employing the different electrolytes were operated using the Aurbach protocol.[36,37] A reservoir lithium layer with a capacity of 4 mAh cm^{-2} was deposited onto a copper foil at a current density of 0.1 mA cm^{-2}. Following this, plating and stripping processes were conducted at a current density of 1 mA cm^{-2} for nine cycles. Subsequently, all the lithium was stripped at 0.1 mA cm^{-2} until the cell potential reached 1.0 V. The **Py13FSI** + **FDG** cell demonstrates the highest CE of 98.9% among the Li||Cu cells using the three different electrolytes, while the other two cells showed lower CEs of 96.4% and 97.8% using **Py13FSI** and **Py13FSI** + **TTE**, respectively. The **Py13FSI** + **DG** electrolyte was not able to complete the protocol in Li||Cu cells due to the occurrence of severe side reactions. The results of the Li||Cu cell tests well agreed with the galvanostatic cycling results, revealing that **Py13FSI** + **FDG** outperformed the other three electrolytes, showing suppressed side reactions as evidenced by the higher CE. The **Py13FSI** + **TTE** and **Py13FSI** + **FDG** cells outperformed the neat **Py13FSI** cell in terms of the CE, which was possibly due to the reduced viscosity upon mixing with the cosolvents as diluents. Despite the lower viscosity in **Py13FSI** + **TTE**, its lower CE than **Py13FSI** + **FDG** could stem from the more significant aluminum corrosion that occurred, as evidenced by the higher leakage current shown in the potentiostatic hold experiments (Fig. S4, ESI†). In terms of lithium-ion transport, although the addition of cosolvents reduced the overall conductivities (Fig. S5 and S6, ESI†) of the electrolytes since **Py13FSI** itself is conductive, the **Py13FSI** + **FDG** electrolyte exhibited a lithium transference number (t^+_{Li}) of 0.73, which was significantly higher than that of the **Py13FSI** electrolyte (t^+_{Li} = 0.53) (Fig. S7, ESI†). The enhanced Li transport in the **Py13FSI** + **FDG** electrolyte could be one of the reasons for the more efficient lithium plating/stripping, and thus the better cycling performance (*vide infra*). The significant increase in the transference number of the **Py13FSI** + **FDG** electrolyte may arise from FDG's moderate solvating ability—primarily through its

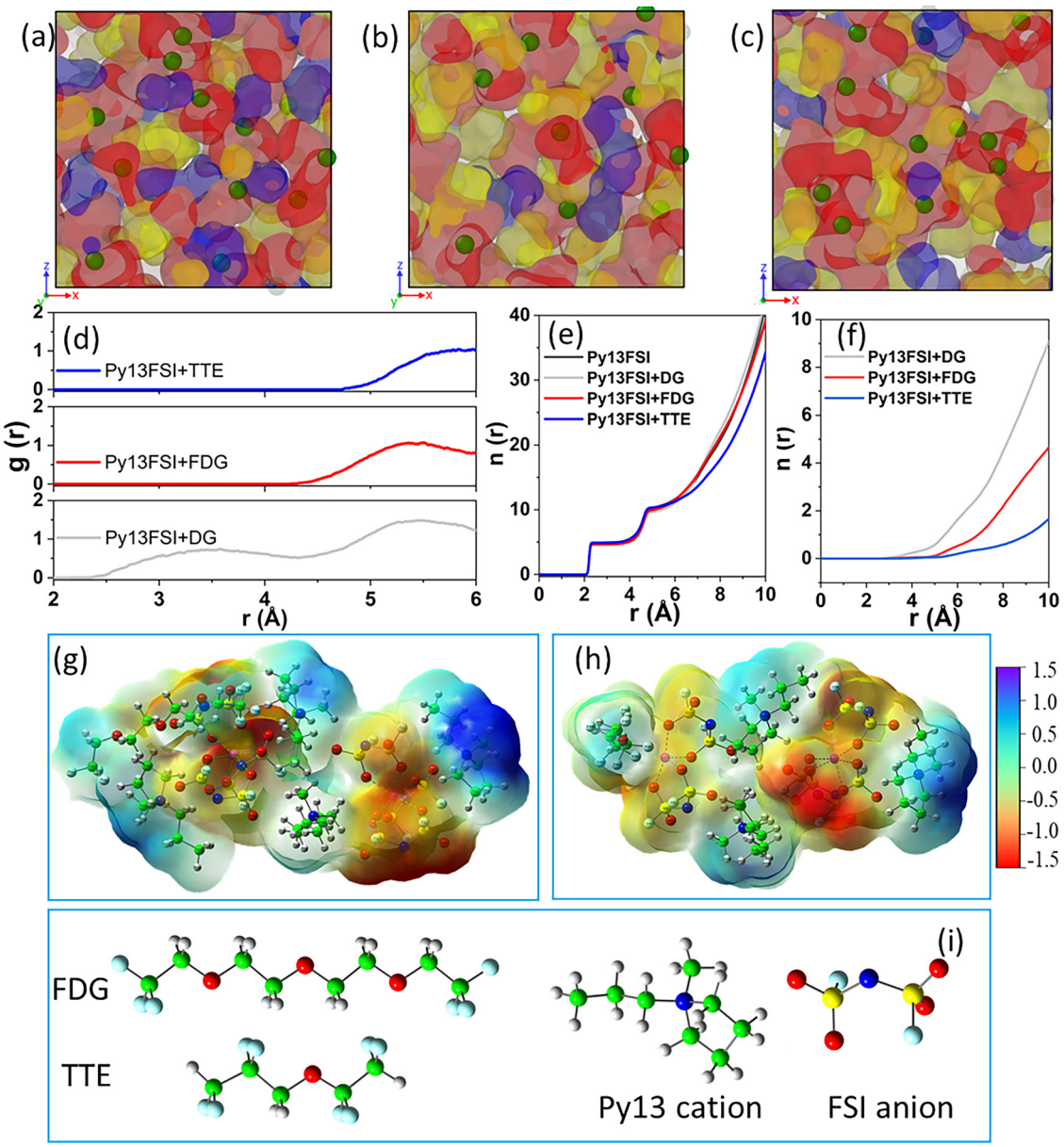

Fig. 3 MD simulation boxes output for the (a) **Py13FSI** + **DG**, (b) **Py13FSI** + **FDG**, and (c) **Py13FSI** + **TTE** electrolytes. Green spheres and red, yellow, and blue clouds represent for Li ions, FSI anions, Py13 cations, and cosolvents. Plots of (d) the radial distribution functions of Li–O_{cosolv}, (e) cumulative number analysis of Li–O_{FSI}, for electrolytes mixed with different cosolvents, and (f) cumulative number analysis of Li–O_{cosolv}. *Ab initio*-Optimized structures showing their sheaths' **MEP** (color scales in volts) of (g) a cluster constructed with four **Py13FSI**, two LiFSI, and one **FDG** molecule depicting the typical solvation sheath structure of the **Py13FSI** + **FDG** electrolyte, and (h) a cluster constructed with three **Py13FSI**, two LiFSI, and one **TTE** molecules, representing the **Py13FSI** + **TTE** electrolyte. (i) Ball–stick model of the molecular structures used in the *ab initio* optimization. All simulations are based on the formulation 1.4 m LiFSI in **Py13FSI**:cosolvent (4 : 1 v/v).

central oxygen, which has higher electron density than the two terminal oxygens adjacent to trifluoromethyl groups. This solvation can weaken Li–FSI interactions (especially given the excess of FSI anions over Li^+ ions), allowing more free Li^+ to act as mobile charge carriers. In contrast, the addition of **TTE**, a non-solvating cosolvent, does not significantly alter the transference number. The unchanged transference number when using **DG** as a cosolvent could be attributed to its much stronger lithium solvation ability compared to **Py13FSI**, making DG the dominant coordinating solvent for LiFSI. Consequently, the ionic liquid no longer forms Li^+–FSI^- clusters but instead serves as a weakly solvating background medium.

FDG-enabled stable cycling of Li||NMC811 cells using the Py13FSI-based electrolyte

Evaluation of the electrochemical stabilities of the four electrolytes was carried out in cells with an NMC 811 cathode and Li anode. The cells were cycled at C/2 after three formation cycles at C/10 with the cutoff voltages being 3.0 and 4.3 V (Fig. 5a). Among these formulations, **Py13FSI** + **FDG** demonstrated a

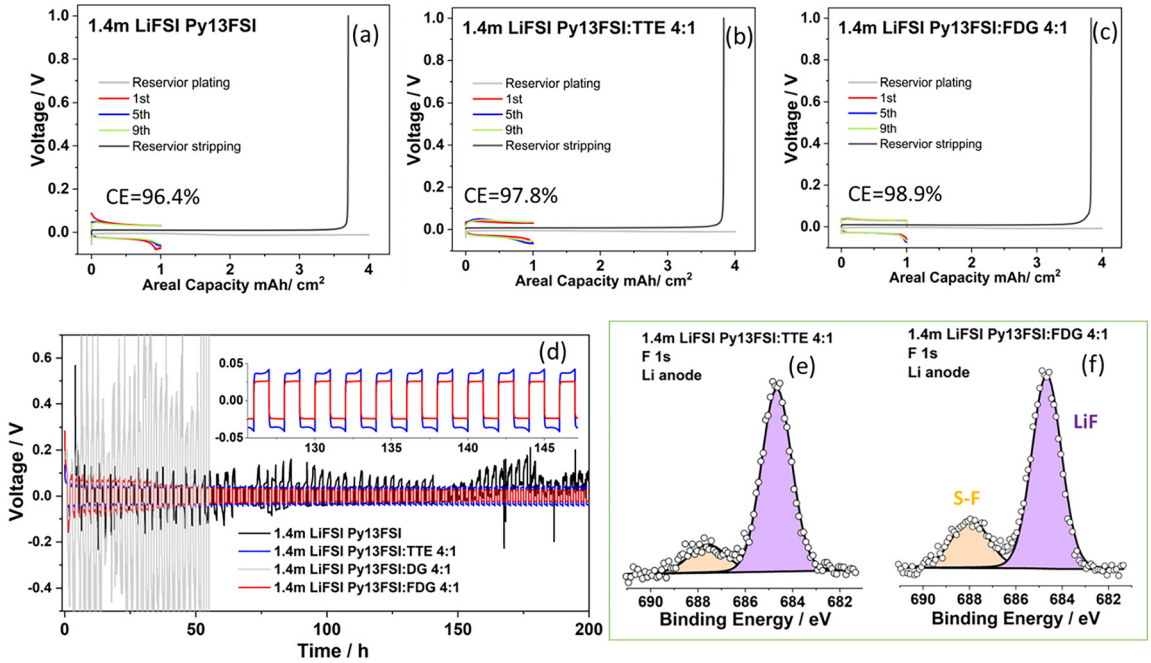

Fig. 4 Voltage profiles over selected cycles for Li||Cu cells containing the different electrolytes studied herein, *i.e.*, (a) **Py13FSI**, (b) **Py13FSI** + **TTE**, and (c) **Py13FSI** + **FDG**. All the Li||Cu cells were cycled according to the Auerbach protocol. (d) Voltage profiles of Li||Li symmetrical cells with the targeted electrolytes; F 1s XPS spectra from the Li anode cycled in (e) **Py13FSI** + **TTE** (f) **Py13FSI** + **FDG** electrolytes in Li||NMC cells.

persistently stable capacity throughout the first 200 cycles and a notable improvement in capacity retention of 95% (156 mAh g^{-1}) at 250 cycles, compared to the pristine **Py13FSI** electrolyte (14%, 25 mAh g^{-1}). The cell using the **Py13FSI** electrolyte without any cosolvent remained stable for only 50 cycles, and showed a rapid capacity decay beginning after 50 cycles. Moreover, the addition of **TTE** as a cosolvent was investigated, which exhibited an enhanced capacity retention of 83 mAh g^{-1} after 250 cycles. However, prior to the continuous capacity drop after 75 cycles, a noticeable first-stage capacity decay from 184 to 162 mAh g^{-1} appeared from the 40th to 75th cycles, which was close to the decay point of the **Py13FSI** cell. Therefore, the similar capacity decay starting points of the **Py13FSI** and **Py13FSI** + **TTE** cells indicated that using **TTE** as a cosolvent did not sufficiently stabilize the Li||NMC811 cell to avoid the first-stage capacity decay (between 40th–75th cycles), although it could still alleviate the rapid capacity drop after 75 cycles, which was observed in the **Py13FSI** cell. In contrast to the other three formulations, the introduction of **DG** resulted in a rapid capacity dip starting already from the 2nd cycle, indicating the low stability and severe side reactions of the electrolyte.

Analyzing selected voltage profiles after various cycles can offer deep insights into the evolving electrochemical behavior of electrolytes over the course of cycling. As shown in Fig. 5b–d and Fig. S3 (ESI†), the four electrolytes provided first-cycle discharge capacities of 183, 189, 181, and 157 mAh g^{-1} for **Py13FSI**, **Py13FSI** + **TTE**, **Py13FSI** + **FDG**, and **Py13FSI** + **DG** cells, respectively. The first-cycle discharge capacity of the **Py13FSI** + **TTE** cell, recorded at 189 mAh g^{-1}, outperformed the other electrolytes, but showed significant capacity fading after 100 cycles, with a capacity of 118 mAh g^{-1} after 200 cycles (Fig. 5c). In comparison, **Py13FSI** exhibited a quicker apparent capacity depletion at earlier cycles than **Py13FSI** + **TTE**. Despite its slightly lower first-cycle capacity, the overall capacity retention of **Py13FSI** + **FDG** outperformed the other formulations, providing a specific capacity of 166 mAh g^{-1} (92% of peak discharge capacity) after 200 cycles (Fig. 5d). The deviation of the voltage profiles from the original formulations other than **Py13FSI** + **FDG** showed the deteriorating cycling stability of the IL-based electrolytes without an appropriate cosolvent present.

The coulombic efficiency (CE) (Fig. 5a) of the Li||NMC811 cells reflects the reversibility of the lithium plating/stripping process in the designated electrolyte environments, as irreversibility is primarily attributed to the electrochemical stabilities of electrolytes against the lithium metal anode.[38,39] As summarized in Table S1 (ESI†), the average CEs in the first 200 cycles for the three cells using **Py13FSI**, **Py13FSI** + **TTE**, and **Py13FSI** + **FDG** were 99.15%, 99.79%, and 99.74%, respectively. The leakage current of Li||NMC cells collected from potentiostatic hold experiments (Fig. S8, ESI†) also confirmed that the **FDG** cosolvent did not compromise the anodic stability at voltages up to 4.6 V, despite its oxidative potential being relatively lower than that of **TTE**. Besides having the highest average CE, **Py13FSI** + **FDG** also demonstrated the most stable cycling, without noticeable decay or deviation points in CE, as were evident with its counterparts (Fig. 5a). Such an observation indicated the enhanced electrolyte stability and reversibility of the Li plating/stripping process enabled by the incorporation of **FDG** as a cosolvent. However, it should be noted that in the current

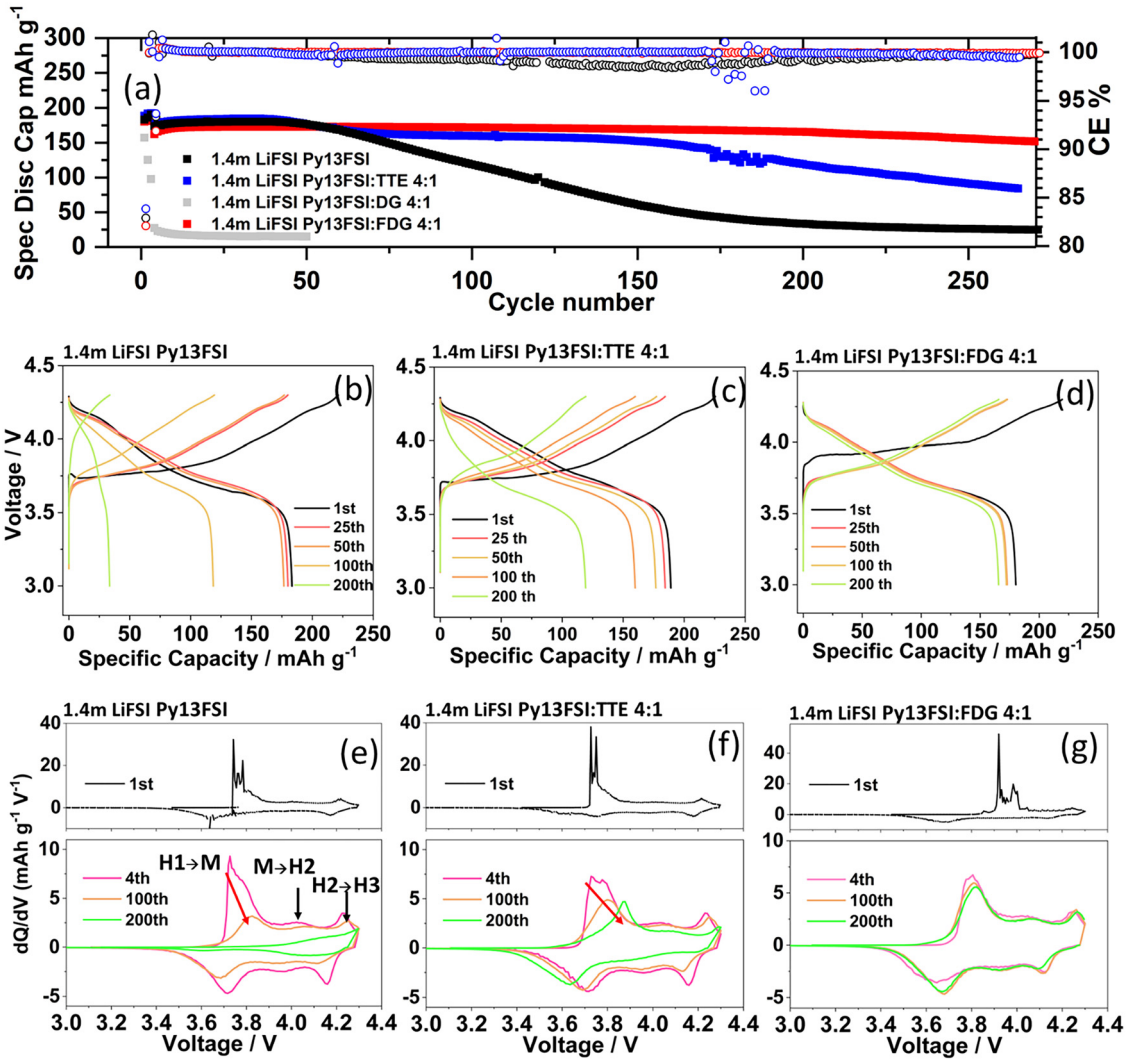

Fig. 5 (a) Evolution of the discharge capacity and CE of Li||NMC811 cells containing different electrolytes. The cells were cycled at C/3 with cutoff voltages of 3.0 and 4.3 V. (b)–(d) Selected voltage–capacity curves of Li||NMC811 cells with different electrolytes at certain cycles. Differential capacity curves at selected cycles in Li||NMC811 cells using (e) **Py13FSI**, (f) **Py13FSI** + **TTE**, (g) **Py13FSI** + **FDG** electrolytes.

electrolyte system, increasing the volumetric ratio of **FDG** did not further extend the cycling life of the Li||NMC cell (Fig. S9, ESI†), possibly due to the higher extent of side reactions from the decomposition of Li–**FDG** clusters. The low cosolvent ratio also guarantees the non-flammability nature of **Py13FSI** would be well retained in the electrolyte solution, which was proven by ignition tests, as shown in Fig. S10 (ESI†).

Robust cathode–electrolyte interphase initiated by FDG as a cosolvent

To gain insights into the electrochemical processes occurring between the electrolytes and NMC811, we created differential capacity (dQ/dV) plots, as displayed in Fig. 5e–g. The NMC811 cathode displayed three characteristic redox peaks at about 3.7, 4.0, and 4.2 V, assigned to the Li intercalation process in three stages: phase transition from a hexagonal (H1) to monoclinic (M) lattice, M to hexagonal (H2), and H2 to hexagonal (H3).[40–42] For both **Py13FSI** and **Py13FSI** + **TTE**, the differential capacity plots (Fig. 5e and f) of the first cycle (*i.e.*, a formation cycle at C/10) did not show a significant potential difference in contrast to the fourth cycle (*i.e.*, the first cycle at C/3). However, the NMC811 cathode in the **Py13FSI** + **FDG** cell displayed an overpotential of 0.1 V compared with the fourth cycle (*i.e.*, 3.9 V in the 1st cycle and 3.8 V for the 4th cycle), which suggested the formation of a passivation layer on the cathode with this electrolyte. The prompt alleviation of the overpotential since the 2nd cycle (Fig. S11, ESI†) indicated that the construction of the desired interphase facilitated lithium intercalation and deintercalation in the cathode. This was further confirmed by the XPS results (Fig. 6) showing the distinct CEI components of the **FDG** electrolyte from the other three electrolytes. With the poorest cycling results, the **Py13FSI** + **DG** cell (Fig. S12, ESI†) showed obvious polarization in the third cycle and crowded spikes for the fourth, indicating severe side reactions and degradation of the electrolyte.

Compared with the initial cycles, a dramatic diminishing of the H1 → M peak and an overpotential of 0.1 V (3.7 to 3.8 V)

were observed after 100 cycles in the Li||NMC811 cell using the **Py13FSI** electrolyte, wherein the H2 → H3 peaks were attenuated as well. As cycling progressed to 200 cycles, the redox features related to the H1 → M and M → H2 transitions completely vanished, and a further faded H2 → H3 signal with a higher overpotential of 0.2 V was observed. The shift and attenuation of the signature phase-transition signals indicated a pronounced irreversibility of these reactions in these cells.[43] In contrast, the H1 → M phase transition of the cell employing **Py13FSI** + **TTE** as the electrolyte after 200 cycles showed a comparable intensity to that of the 100th cycle, although a higher overpotential at 3.9 V was still observed. The M → H2 phase intensity was mostly retained at 200 cycles whereas the H2 → H3 phase decayed significantly, which was similar to the case of the **Py13FSI** cell. With the best capacity retention in this work, the **Py13FSI** + **FDG** cell retained all three phase-transformation signals intact, without any noticeable overpotential or intensity decay (Fig. 5g). Since the XRD patterns collected from the cycled cathodes confirmed the intact nature of the NMC materials in all the electrolytes (Fig. S13, ESI†), the overpotential built during cycling was attributed to detrimental interphases formed between the cathode and the given electrolytes. As can be seen in Fig. 5f, the remaining transition signals related to the H1 → M and M → H2 transitions (compared with the **Py13FSI** electrolyte in Fig. 5e) suggested that the use of **TTE** as a cosolvent could help stabilize Li^+ intercalation during such phase transition to some extent. In the **Py13FSI** + **FDG** case, the overpotential-free characteristic even at 200 cycles verified that the interphase in this case was robust and favorable for Li^+ cation transport.[44] Unlike the other three cells that were capable of being cycled over 100 times, the instability of the **Py13FSI** + **DG** electrolyte was also reflected in the dQ/dV curve (Fig. S14, ESI†), which showed the loss of all the phase-transition peaks at the 4th cycle. This could stem from the strong solvation of **DG** with Li^+, resulting in a solvation sheath that was not favorable for the formation of robust interphases, which will be further discussed in the solvation section.

To probe the formation of interphases as a function of the electrolyte formulation, we performed electrochemical impedance spectroscopy (EIS) analysis of Li||NMC cells after the interphase formation cycles to monitor the impedance of the interphases. The EIS data (Fig. S15a, ESI†) in the frequency range from 500 kHz to 120 Hz (*i.e.*, the first arch in the Nyquist plot in this work) reflected the resistance of the interphase film at the surface of the electrodes.[24] As shown in the spectra, the Li||NMC cell with **Py13FSI** + **FDG** as the electrolyte showed the lowest interphase resistance among the three tested electrolytes, whereas the absence of any cosolvent in the **Py13FSI** electrolyte resulted in its largest interphase resistance. The progressive establishment of the interphase between the electrolytes and electrodes during repeated Li^+ de-/intercalation using the different electrolytes can cause distinct charge-transfer kinetics that will further affect the long-term electrochemical performance of the cells.[43,45] Note that the EIS measurements in this work did not distinguish the detailed interfacial electrochemistry occurring on the cathode and anode interfaces individually. However, the EIS measurements in the symmetric Li||Li cells (Fig. S15b, ESI†) after 15 cycles at 1 mA cm^{-2} displayed similar interphase resistances (reflected by the first arch in the Nyquist plot) on the Li surface across the three electrolytes, which suggests similar properties of the interphases formed on the Li surface. This observation corroborated the XPS results for the SEI in the presence of the different electrolytes (*vide infra*). Therefore, we attribute such interfacial-resistance difference observed in Li||NMC cells to the different cathode interphase formations caused by varying the cosolvent. The cathode interphase with a low resistance established in **Py13FSI** + **FDG** favored lithium transport as cycling progressed, which aligned with the stable overpotential at high cycle numbers shown in Fig. 3f.

Distinct solvation structures, by influencing the species distribution within the inner or secondary sheath, can lead to different interfacial processes occurring between the electrolyte components and electrodes (*i.e.*, either cathode, anode or both). We thus studied the surface chemistry of the electrodes after cycling by X-ray photoelectron spectroscopy (XPS) (Fig. 4e, f and 6, and Table S2, ESI†). On the lithium anode surface (Fig. 4e and f), two major components, SO_2–F and LiF at 687.5 and 684.5 eV, respectively, were identified from the deconvoluted F1s spectra collected from the cells with **Py13FSI** and **Py13FSI** + **FDG**. The presence of SO_2–F and LiF species suggest that the SEI was mainly formed from the decomposition of FSI

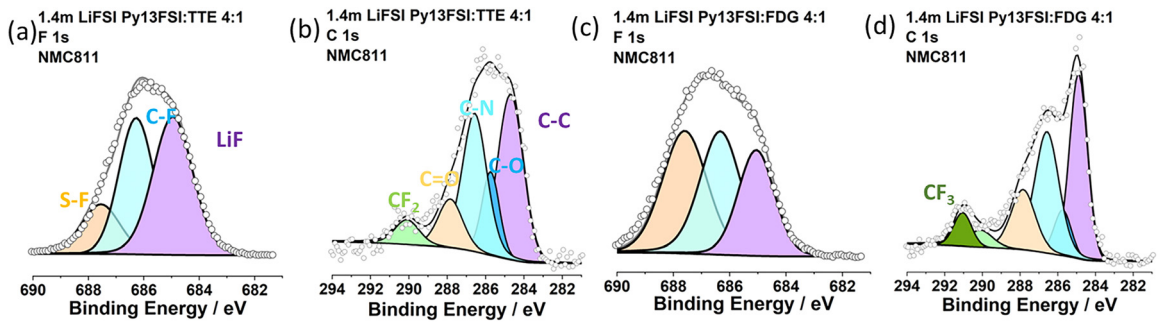

Fig. 6 Deconvoluted XPS results collected from the NMC811 cathode dissembled from cells filled with the **Py13FSI** + **FDG** and **Py13FSI** + **TTE** electrolytes after cycling tests. (a) F 1s and (b) C 1s spectra from the NMC cathode cycled in the **Py13FSI** + **TTE** electrolyte. (c) F 1s and (d) C 1s spectra from the NMC811 cathode cycled in the **Py13FSI** + **FDG** electrolyte.

anions in both electrolytes. The addition of 20% (volume) **FDG** did not result in significant changes in the anode-surface components other than a slight increase in the SO_2–F content (*i.e.* 24.2% in **Py13FSI** + **FDG** cells) compared to in **Py13FSI** + **TTE** (16.3%) and **Py13FSI** (22.5%) (Fig. 4e, f and Fig. S16, and Table S2, ESI†). Note that no noticeable C–F species, which could arise from the decomposition of **FDG** or **TTE**, were identified on the anode surface. The similar XPS profiles collected from the anodes for all three electrolytes indicated there were only moderate changes in the SEI when adding the cosolvents, which was in good agreement with the EIS results collected from Li||Li cells after cycling at 1 mA cm^{-2} for 15 cycles, where similar interphase (SEI) resistances were observed for all three cases (Fig. S15b, ESI†). The moderate changes in SEI species among the three electrolytes were due to the high concentration (relatively higher than commonly used 1 M LiFSI) of FSI anions, which are more prone to decompose to form a stable SEI than ethereal cosolvents, which corroborates with the two identified species (Fig. 4e and f) indicating FSI decomposition.[17,20] On the cathode side, however, the addition of **FDG** led to an interphase containing noticeably more SO_2–F from FSI decomposition, as observed in the F 1s spectra in Fig. 6, compared to **Py13FSI** and **Py13FSI** + **TTE**. Furthermore, the C 1s spectra on the cathode retrieved from the cells with **Py13FSI** + **FDG** as the electrolyte revealed the presence of 6% of CF_3 species (291 eV, Fig. 6d), which we supposed were generated from the oxidative degradation of **FDG**.[46] Differently, CF_2 species at 290 eV (ref. 43) from **TTE** decomposition were not apparent on the cathode, as evidenced by the similar C–F contents in the F 1s and C 1s XPS spectra (Fig. 6a and b) compared to **Py13FSI** (Fig. S16, ESI†). These findings are intriguing since MD simulations revealed negligible differences in the FSI quantities within the inner solvation sheath (2.0–2.4 Å), whereas the introduction of cosolvents apparently altered the interfacial chemistry through FSI degradation at the cathode surface. We believe that the properties of the shell in the medial range to Li^+ (4–10 Å) where the nearest cosolvent molecules reside, determined by the solvation capabilities of cosolvents, could be critical for the occurrence of such different surface behaviors on the cathode. Taking these observations together, it is clear that the generation of more organic species (SO_2–F and C–F) from the decomposition of **FDG** and FSI- in the **Py13FSI** + **FDG** electrolyte is crucial for the stabilization of the cathode–electrolyte interphase. Such an interphase with optimal physical and electrochemical properties can facilitate lithium intercalations with suppressed overpotential (Fig. 4a–c) and side reactions.

Conclusion

In this study, we found that **FDG**, when used as a cosolvent in ionic-liquid-based electrolytes, significantly extended the cycling life of the **Py13FSI** electrolyte. Electrochemical and surface analyses confirmed that this improvement resulted from the formation of a favorable cathode interphase, which enabled efficient Li^+ transport with a reduced overpotential. Spectroscopic analyses, including FTIR, Raman, and NMR, as well as MD simulations, revealed the different solvation structures in **Py13FSI**-based electrolytes when adding cosolvents with varying solvation abilities. The mild solvating strength and lithium stability of **FDG** were found to be key factors behind its success. In contrast, **DG**, a strong solvating solvent, dramatically altered the solvation shell of the ionic liquid electrolyte, making the **Py13FSI–DG** electrolyte unstable at the lithium metal anode. On the other hand, **TTE**, which is a non-solvating solvent, failed to enhance lithium transport in the **Py13FSI–TTE** electrolyte and did not form a stable interphase on the cathode surface. Thus, **FDG**, with its balanced solvating properties, provides the optimal solution. Our comparisons with **TTE** and **DG** showed that a medium-range solvation shell is crucial for facilitating the formation of a stable electrolyte–cathode interphase, potentially through FSI decomposition. This work should help guide the future development of long-lasting ionic liquid-based electrolytes.

Conflicts of interest

The authors declare no competing financial interest.

Data availability

The data that support the findings of this study are available from the corresponding author upon reasonable request.

Acknowledgements

This work was conducted as part of the U.S.-German joint collaboration on ''Interfaces and Interphases in Rechargeable Li-metal Based Batteries'' supported by the U.S. Department of Energy (DOE) and the German Federal Ministry of Education and Research (BMBF). Financial support was provided by the U.S. Department of Energy (DOE), Vehicle Technologies Office (VTO). Argonne National Laboratory is operated for the DOE Office of Science by UChicago Argonne, LLC, under the contract number DE-AC02-06CH11357 under the U.S.-Germany Cooperation on Energy Storage. The NMC electrodes were manufactured at the DOE's CAMP Facility, Argonne National Laboratory. The CAMP Facility is fully supported by the DOE VTO within the core funding of the Applied Battery Research for Transportation Program. P.B.B. and J.M.S. acknowledge the DOE through the US–Germany Cooperation on Energy Storage under Contract DE-AC02-05CH11357. Z.L. and D.B. acknowledge the financial support from the Helmholtz Association and the BMBF within the LILLINT-2 project (03XP0511E). Computational resources from Texas A&M University High Performance Research Computing are gratefully acknowledged.

References

1 X.-B. Cheng, R. Zhang, C.-Z. Zhao and Q. Zhang, Toward Safe Lithium Metal Anode in Rechargeable Batteries: A Review,

Chem. Rev., 2017, **117**(15), 10403–10473, DOI: 10.1021/acs.chemrev.7b00115.

2 D. Lin, Y. Liu and Y. Cui, Reviving the lithium metal anode for high-energy batteries, *Nat. Nanotechnol.*, 2017, **12**(3), 194–206, DOI: 10.1038/nnano.2017.16.

3 X. Ren, L. Zou, X. Cao, M. H. Engelhard, W. Liu, S. D. Burton, H. Lee, C. Niu, B. E. Matthews and Z. Zhu, *et al.*, Enabling High-Voltage Lithium-Metal Batteries under Practical Conditions, *Joule*, 2019, **3**(7), 1662–1676, DOI: 10.1016/j.joule.2019.05.006.

4 Y. Zhao, T. Zhou, T. Ashirov, M. E. Kazzi, C. Cancellieri, L. P. H. Jeurgens, J. W. Choi and A. Coskun, Fluorinated ether electrolyte with controlled solvation structure for high voltage lithium metal batteries, *Nat. Commun.*, 2022, **13**(1), 2575, DOI: 10.1038/s41467-022-29199-3.

5 Z. Yu, H. Wang, X. Kong, W. Huang, Y. Tsao, D. G. Mackanic, K. Wang, X. Wang, W. Huang and S. Choudhury, *et al.*, Molecular design for electrolyte solvents enabling energy-dense and long-cycling lithium metal batteries, *Nat. Energy*, 2020, **5**(7), 526–533, DOI: 10.1038/s41560-020-0634-5.

6 W. Zhao, J. Zheng, L. Zou, H. Jia, B. Liu, H. Wang, M. H. Engelhard, C. Wang, W. Xu and Y. Yang, *et al.*, High Voltage Operation of Ni-Rich NMC Cathodes Enabled by Stable Electrode/Electrolyte Interphases, *Adv. Energy Mater.*, 2018, **8**(19), 1800297, DOI: 10.1002/aenm.201800297(acccessed 2024/04/29).

7 Z. Zhang, J. Yang, W. Huang, H. Wang, W. Zhou, Y. Li, Y. Li, J. Xu, W. Huang and W. Chiu, *et al.*, Cathode-Electrolyte Interphase in Lithium Batteries Revealed by Cryogenic Electron Microscopy, *Matter*, 2021, **4**(1), 302–312, DOI: 10.1016/j.matt.2020.10.021.

8 A. Heist, S. Hafner and S.-H. Lee, High-Energy Nickel-Rich Layered Cathode Stabilized by Ionic Liquid Electrolyte, *J. Electrochem. Soc.*, 2019, **166**(6), A873, DOI: 10.1149/2.0071906jes.

9 H. Wu, H. Jia, C. Wang, J.-G. Zhang and W. Xu, Recent Progress in Understanding Solid Electrolyte Interphase on Lithium Metal Anodes, *Adv. Energy Mater.*, 2021, **11**(5), 2003092, DOI: 10.1002/aenm.202003092(acccessed 2024/04/29).

10 X.-B. Cheng, R. Zhang, C.-Z. Zhao, F. Wei, J.-G. Zhang and Q. Zhang, A Review of Solid Electrolyte Interphases on Lithium Metal Anode, *Adv. Sci.*, 2016, **3**(3), 1500213, DOI: 10.1002/advs.201500213(acccessed 2024/04/29).

11 X. Fan and C. Wang, High-voltage liquid electrolytes for Li batteries: progress and perspectives, *Chem. Soc. Rev.*, 2021, **50**(18), 10486–10566, DOI: 10.1039/D1CS00450F.

12 Y. Wang, Z. Li, Y. Hou, Z. Hao, Q. Zhang, Y. Ni, Y. Lu, Z. Yan, K. Zhang and Q. Zhao, *et al.*, Emerging electrolytes with fluorinated solvents for rechargeable lithium-based batteries, *Chem. Soc. Rev.*, 2023, **52**(8), 2713–2763, DOI: 10.1039/D2CS00873D.

13 X. Ren, L. Zou, S. Jiao, D. Mei, M. H. Engelhard, Q. Li, H. Lee, C. Niu, B. D. Adams and C. Wang, *et al.*, High-Concentration Ether Electrolytes for Stable High-Voltage Lithium Metal Batteries, *ACS Energy Lett.*, 2019, **4**(4), 896–902, DOI: 10.1021/acsenergylett.9b00381.

14 J. Alvarado, M. A. Schroeder, T. P. Pollard, X. Wang, J. Z. Lee, M. Zhang, T. Wynn, M. Ding, O. Borodin and Y. S. Meng, *et al.*, Bisalt ether electrolytes: a pathway towards lithium metal batteries with Ni-rich cathodes, *Energy Environ. Sci.*, 2019, **12**(2), 780–794, DOI: 10.1039/C8EE02601G.

15 L. E. Camacho-Forero, T. W. Smith and P. B. Balbuena, Effects of High and Low Salt Concentration in Electrolytes at Lithium–Metal Anode Surfaces, *J. Phys. Chem. C*, 2017, **121**(1), 182–194, DOI: 10.1021/acs.jpcc.6b10774.

16 S. Jiao, X. Ren, R. Cao, M. H. Engelhard, Y. Liu, D. Hu, D. Mei, J. Zheng, W. Zhao and Q. Li, *et al.*, Stable cycling of high-voltage lithium metal batteries in ether electrolytes, *Nat. Energy*, 2018, **3**(9), 739–746, DOI: 10.1038/s41560-018-0199-8.

17 S. Chen, J. Zheng, D. Mei, K. S. Han, M. H. Engelhard, W. Zhao, W. Xu, J. Liu and J.-G. Zhang, High-Voltage Lithium-Metal Batteries Enabled by Localized High-Concentration Electrolytes, *Adv. Mater.*, 2018, **30**(21), 1706102, DOI: 10.1002/adma.201706102(acccessed 2023/08/14).

18 X. Ren, S. Chen, H. Lee, D. Mei, M. H. Engelhard, S. D. Burton, W. Zhao, J. Zheng, Q. Li and M. S. Ding, *et al.*, Localized High-Concentration Sulfone Electrolytes for High-Efficiency Lithium-Metal Batteries, *Chem*, 2018, **4**(8), 1877–1892, DOI: 10.1016/j.chempr.2018.05.002.

19 S. Perez Beltran, X. Cao, J.-G. Zhang and P. B. Balbuena, Localized High Concentration Electrolytes for High Voltage Lithium–Metal Batteries: Correlation between the Electrolyte Composition and Its Reductive/Oxidative Stability, *Chem. Mater.*, 2020, **32**(14), 5973–5984, DOI: 10.1021/acs.chemmater.0c00987.

20 X. Cao, H. Jia, W. Xu and J.-G. Zhang, Review—Localized High-Concentration Electrolytes for Lithium Batteries, *J. Electrochem. Soc.*, 2021, **168**(1), 010522, DOI: 10.1149/1945-7111/abd60e.

21 N. Karimi, M. Zarrabeitia, A. Mariani, D. Gatti, A. Varzi and S. Passerini, Nonfluorinated Ionic Liquid Electrolytes for Lithium Metal Batteries: Ionic Conduction, Electrochemistry, and Interphase Formation, *Adv. Energy Mater.*, 2021, **11**(4), 2003521, DOI: 10.1002/aenm.202003521(acccessed 2024/04/29).

22 Z. Wang, F. Zhang, Y. Sun, L. Zheng, Y. Shen, D. Fu, W. Li, A. Pan, L. Wang and J. Xu, *et al.*, Intrinsically Nonflammable Ionic Liquid-Based Localized Highly Concentrated Electrolytes Enable High-Performance Li-Metal Batteries, *Adv. Energy Mater.*, 2021, **11**(17), 2003752, DOI: 10.1002/aenm.202003752(acccessed 2024/04/29).

23 H. Sun, G. Zhu, Y. Zhu, M.-C. Lin, H. Chen, Y.-Y. Li, W. H. Hung, B. Zhou, X. Wang and Y. Bai, *et al.*, High-Safety and High-Energy-Density Lithium Metal Batteries in a Novel Ionic-Liquid Electrolyte, *Adv. Mater.*, 2020, **32**(26), 2001741, DOI: 10.1002/adma.202001741(acccessed 2024/04/29).

24 Q. Liu, W. Jiang, J. Xu, Y. Xu, Z. Yang, D.-J. Yoo, K. Z. Pupek, C. Wang, C. Liu and K. Xu, *et al.*, A fluorinated cation introduces new interphasial chemistries to enable high-voltage lithium metal batteries, *Nat. Commun.*, 2023, **14**(1), 3678, DOI: 10.1038/s41467-023-38229-7.

25 D.-J. Yoo, K. J. Kim and J. W. Choi, The Synergistic Effect of Cation and Anion of an Ionic Liquid Additive for Lithium

Metal Anodes, *Adv. Energy Mater.*, 2018, **8**(11), 1702744, DOI: 10.1002/aenm.201702744(acccessed 2024/04/29).

26 M. Hasanpoor, M. Eftekharnia, T. Pathirana, U. Pal, R. Kerr, M. Forsyth and P. C. Howlett, Understanding the Role of Separator and Electrolyte Compatibility on Lithium Metal Anode Performance Using Ionic Liquid-Based Electrolytes, *ACS Appl. Energy Mater.*, 2021, **4**(6), 6310–6323, DOI: 10.1021/acsaem.1c01114.

27 Q. Zhou, W. A. Henderson, G. B. Appetecchi, M. Montanino and S. Passerini, Physical and Electrochemical Properties of N-Alkyl-N-methylpyrrolidinium Bis(fluorosulfonyl)imide Ionic Liquids: PY13FSI and PY14FSI, *J. Phys. Chem. B*, 2008, **112**(43), 13577–13580, DOI: 10.1021/jp805419f.

28 S. P. Ong, O. Andreussi, Y. Wu, N. Marzari and G. Ceder, Electrochemical Windows of Room-Temperature Ionic Liquids from Molecular Dynamics and Density Functional Theory Calculations, *Chem. Mater.*, 2011, **23**(11), 2979–2986, DOI: 10.1021/cm200679y.

29 X. Liu, A. Mariani, T. Diemant, M. E. D. Pietro, X. Dong, M. Kuenzel, A. Mele and S. Passerini, Difluorobenzene-Based Locally Concentrated Ionic Liquid Electrolyte Enabling Stable Cycling of Lithium Metal Batteries with Nickel-Rich Cathode, *Adv. Energy Mater.*, 2022, **12**(25), 2200862, DOI: 10.1002/aenm.202200862(acccessed 2024/04/29).

30 S. Lee, K. Park, B. Koo, C. Park, M. Jang, H. Lee and H. Lee, Safe, Stable Cycling of Lithium Metal Batteries with Low-Viscosity, Fire-Retardant Locally Concentrated Ionic Liquid Electrolytes, *Adv. Funct. Mater.*, 2020, **30**(35), 2003132, DOI: 10.1002/adfm.202003132(acccessed 2024/04/29).

31 X. Liu, A. Mariani, T. Diemant, X. Dong, P.-H. Su and S. Passerini, Locally Concentrated Ionic Liquid Electrolytes Enabling Low-Temperature Lithium Metal Batteries, *Angew. Chem., Int. Ed.*, 2023, **62**(31), e202305840, DOI: 10.1002/anie.202305840(acccessed 2024/04/29).

32 O. Borodin, W. Gorecki, G. D. Smith and M. Armand, Molecular Dynamics Simulation and Pulsed-Field Gradient NMR Studies of Bis(fluorosulfonyl)imide (FSI) and Bis[(trifluoromethyl)-sulfonyl]imide (TFSI)-Based Ionic Liquids, *J. Phys. Chem. B*, 2010, **114**(20), 6786–6798, DOI: 10.1021/jp911950q.

33 H. Yoon, A. S. Best, M. Forsyth, D. R. MacFarlane and P. C. Howlett, Physical properties of high Li-ion content N-propyl-N-methylpyrrolidinium bis(fluorosulfonyl)imide based ionic liquid electrolytes, *Phys. Chem. Chem. Phys.*, 2015, **17**(6), 4656–4663, DOI: 10.1039/C4CP05333H.

34 Z. Wang, H. Zhang, R. Han, J. Xu, A. Pan, F. Zhang, D. Huang, Y. Wei, L. Wang and H. Song, *et al.*, Establish an Advanced Electrolyte/Graphite Interphase by an Ionic Liquid-Based Localized Highly Concentrated Electrolyte for Low-Temperature and Rapid-Charging Li-Ion Batteries, *ACS Sustainable Chem. Eng.*, 2022, **10**(36), 12023–12029, DOI: 10.1021/acssuschemeng.2c03938.

35 H. Tu, L. Li, Z. Wang, J. Wang, H. Lin, M. Wang, C. Yan and M. Liu, Tailoring Electrolyte Solvation for LiF-Rich Solid Electrolyte Interphase toward a Stable Li Anode, *ACS Nano*, 2022, **16**(10), 16898–16908, DOI: 10.1021/acsnano.2c06924.

36 X. Li, X. Wu, H. A. Doan, Z. Yang, R. Amine, M. Li, M. V. Bracamonte, C.-C. Su and K. Amine, Acidity-Governed Rules in the Electrochemical Performance of Fluorinated Benzenes for High-Voltage Lithium Metal Batteries, *ACS Energy Lett.*, 2024, **9**(7), 3484–3491, DOI: 10.1021/acsenergylett.4c01215.

37 B. D. Adams, J. Zheng, X. Ren, W. Xu and J.-G. Zhang, Accurate Determination of Coulombic Efficiency for Lithium Metal Anodes and Lithium Metal Batteries, *Adv. Energy Mater.*, 2018, **8**(7), 1702097, DOI: 10.1002/aenm.201702097(acccessed 2024/04/30).

38 S. Ko, T. Obukata, T. Shimada, N. Takenaka, M. Nakayama, A. Yamada and Y. Yamada, Electrode potential influences the reversibility of lithium-metal anodes, *Nat. Energy*, 2022, **7**(12), 1217–1224, DOI: 10.1038/s41560-022-01144-0.

39 H. Liu, X.-B. Cheng, R. Xu, X.-Q. Zhang, C. Yan, J.-Q. Huang and Q. Zhang, Plating/Stripping Behavior of Actual Lithium Metal Anode, *Adv. Energy Mater.*, 2019, **9**(44), 1902254, DOI: 10.1002/aenm.201902254(acccessed 2025/01/16).

40 S. Zheng, C. Hong, X. Guan, Y. Xiang, X. Liu, G.-L. Xu, R. Liu, G. Zhong, F. Zheng and Y. Li, *et al.*, Correlation between long range and local structural changes in Ni-rich layered materials during charge and discharge process, *J. Power Sources*, 2019, **412**, 336–343, DOI: 10.1016/j.jpowsour.2018.11.053.

41 R. Jung, M. Metzger, F. Maglia, C. Stinner and H. A. Gasteiger, Oxygen Release and Its Effect on the Cycling Stability of LiNixMnyCozO2 (NMC) Cathode Materials for Li-Ion Batteries, *J. Electrochem. Soc.*, 2017, **164**(7), A1361, DOI: 10.1149/2.0021707jes.

42 L. de Biasi, A. Schiele, M. Roca-Ayats, G. Garcia, T. Brezesinski, P. Hartmann and J. Janek, Phase Transformation Behavior and Stability of LiNiO2 Cathode Material for Li-Ion Batteries Obtained from *In Situ* Gas Analysis and Operando X-Ray Diffraction, *ChemSusChem*, 2019, **12**(10), 2240–2250, DOI: 10.1002/cssc.201900032(acccessed 2024/04/30).

43 F. Wu, S. Fang, M. Kuenzel, A. Mullaliu, J.-K. Kim, X. Gao, T. Diemant, G.-T. Kim and S. Passerini, Dual-anion ionic liquid electrolyte enables stable Ni-rich cathodes in lithium-metal batteries, *Joule*, 2021, **5**(8), 2177–2194, DOI: 10.1016/j.joule.2021.06.014.

44 J.-H. Kim, S. J. Kim, T. Yuk, J. Kim, C. S. Yoon and Y.-K. Sun, Variation of Electronic Conductivity within Secondary Particles Revealing a Capacity-Fading Mechanism of Layered Ni-Rich Cathode, *ACS Energy Lett.*, 2018, **3**(12), 3002–3007, DOI: 10.1021/acsenergylett.8b02043.

45 Y. Rao, X. Li, S. Zhao, P. Liu, F. Wu, X. Liu, N. Zhou, S. Fang and S. Passerini, Fluorinated electrolyte formulations design enabling high-voltage and long-life lithium metal batteries, *Nano Energy*, 2024, **123**, 109362, DOI: 10.1016/j.nanoen.2024.109362.

46 Q. Liu, J. Xu, W. Jiang, J. Gim, A. P. Tornheim, R. Pathak, Q. Zhu, P. Zuo, Z. Yang and K. Z. Pupek, *et al.*, High-Energy LiNiO2 Li Metal Batteries Enabled by Hybrid Electrolyte Consisting of Ionic Liquid and Weakly Solvating Fluorinated Ether, *Adv. Sci.*, 2024, **11**(46), 2409662, DOI: 10.1002/advs.202409662(acccessed 2025/01/14).

